JPE 16-4-32

http://dx.doi.org/10.6113/JPE.2016.16.4.1587
ISSN(Print): 1598-2092 / ISSN(Online): 2093-4718

A Two State Feedback Active Damping Strategy for the *LCL* Filter Resonance in Grid-Connected Converters

Mahmoud A. Gaafar[†,*], Emad M. Ahmed[*], and Masahito Shoyama[**]

[†,**]Graduate School of Information Science and Electrical Engineering, Kyushu University, Fukuoka, Japan
[*]Department of Electrical Engineering, Faculty of Engineering, Aswan University, Aswan, Egypt

Abstract

A novel active damping strategy for the *LCL* filter resonance is proposed using the grid current and the capacitor voltage. The proposed technique is deduced in the continuous time domain and a discussion for its discrete implementation is presented. According to the proposed technique, instability of the open loop system, which results in non-minimum phase behavior, can be avoided over wide range of resonant frequencies. Moreover, straightforward co-design steps for both the fundamental current regulator and the active damping loops can be used. A numerical example along with experimental results are introduced to validate the proposed strategy performance over wide range of resonant frequencies.

Key words: *LCL* filter, active damping, resonance, converters, grid

I. INTRODUCTION

Due to their higher attenuation for switching harmonics with a lower size and weight, *LCL* filters are widely used with grid-connected converters to limit the harmonic contents of the injected grid current to comply with the grid codes; i.e. IEEE 519-1992 [1]. However, the inherent resonance of the *LCL* filters represents a challenge for control system designers. Damping techniques have to be adopted to cope with this challenge. With discrete implementation, closed loop system stability can be maintained by the inherent damping characteristic of a single grid current control loop for resonant frequencies greater than one-sixth of the control frequency [2]. However, this strategy gives rise instability due to resonant frequency variations which are likely to occur particularly in weak grids where the grid inductance changes significantly [3]. Passive damping, by using a resistor, was used to cope with this issue [4]. However, it causes power losses. Thus active damping (AD) by modifying the control algorithm is preferred [5].

Manuscript received Feb. 3, 2016; accepted Apr. 18, 2016
Recommended for publication by Associate Editor Jinjun Liu.
[†]Corresponding Author: gaafar@ckt.ees.kyushu-u.ac.jp
Tel:+81-92-802-3704, Fax: +81-92-802-3703, Kyushu University
[*]Dept. of Electrical Engineering, Aswan University, Aswan, Egypt
[**]Graduate School of Information Science and Electrical Engineering, Kyushu University, Japan

Number of active damping techniques have been discussed in the literature [6]-[20]. A cascaded filter in the current control loop was used in [6] and [7]. However, this method is highly sensitive to resonant frequency variations. In addition, it causes a reduction in the system bandwidth. To overcome these issues, an inner feedback loop of one of the filter states has been employed to produce a damping effect [8]-[20]. A proportional feedback of the filter capacitor current was employed in [8]-[10]. To stabilize the closed loop system, it was proved that excitation of unstable open loop poles is mandatory for resonant frequencies greater than one-sixth of the control frequency [11]- [12]. This non-minimum phase behavior can decline the system performance especially when selective harmonic mitigation is of concern [11]. Modified feedback loops of the capacitor current have recently been proposed to avoid this behavior over wider range of resonant frequencies [11]-[15]. However, a high precision current sensor or a complicated observer loop is needed [16]. The capacitor voltage differentiation can be used to produce a damping effect. However, this technique results in noise amplification. To cope with this issue, a lead-lag network has been adopted to behave as a differentiator around the resonant frequency [17]- [18]. However, as shown in [17] , this method can be used effectively over limited range of resonant frequencies between 1/3.2 and 1/3.4 of the control frequency.

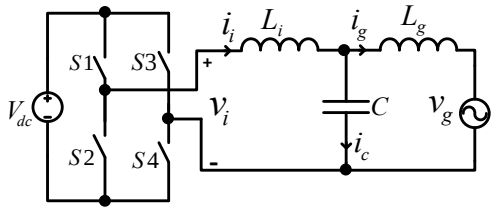

Fig. 1. Grid-connected Single phase inverter through an *LCL* filter.

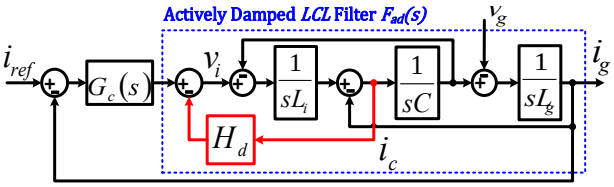

Fig. 2. Block diagram of capacitor-current-based active damping.

Grid-current-based active damping has recently been discussed [19]-[20]. Ideally, this needs an s^2 term which cannot be implemented practically due to noise amplification. A high pass filter (HPF) is employed in [19] instead of the s^2 term. This technique is further discussed in [20] where it was shown that non-minimum phase behavior can be avoided for resonant frequencies up to a theoretical limit of 0.27 of the sampling frequency. However, the co-design steps of this HPF along with the fundamental current regulator are very complicated since many iterations are needed. Moreover, avoiding non-minimum behavior at high resonant frequencies requires increasing the cutoff frequency of the HPF to its maximum practical limit of 0.5 of the sampling frequency (Nyquist frequency). However, using such high value can deteriorate the HPF performance. This in turn, makes it unsuitable for practical implementation. Due to this practical limitation, and during the performance verification presented in [20], non-minimum phase behavior has been avoided up to a maximum resonant frequency of about 0.24 of the sampling frequency.

In this paper, two feedback loops of the grid current and the capacitor voltage are proposed as a new active damping strategy. By using the proposed strategy, the non-minimum phase characteristics can be avoided over a wide range of resonant frequencies. Moreover, straightforward co-design procedures for both the fundamental current regulator and the active damping loops are proposed. For reduced number of sensors, virtual flux technique can be employed to estimate the capacitor voltage [18]. However, this is not adopted here.

Following this introduction, section II presents the continuous time domain derivation of the proposed active damping strategy. In section III, discrete implementation of the proposed strategy is presented along with the co-design steps of the fundamental current regulator and the active damping loops. In section IV, a numerical example along with experimental work are introduced to verify the proposed strategy performance at different resonant frequencies. Finally, section V presents some conclusions.

II. Proposed Active Damping Strategy

A. System Description

Fig. 1 shows a single phase inverter connected to the grid through an *LCL* filter. The block diagram of the capacitor-current-based active damping system is shown in Fig. 2, where a proportional feedback (H_d) of the capacitor current is used to actively damp the filter resonance. The un-damped filter transfer function is denoted as $G_{ig}(s)$ and is expressed in (1), where ω_{res} - expressed in (2) - is the *LCL* filter resonant frequency. A proportional resonant (*PR*) controller with a transfer function of $G_c(s)$ – expressed in (3) – is employed for fundamental current regulation.

$$G_{ig}(s) = \frac{I_g(s)}{V_i(s)} = \frac{1}{L_i L_g C s\left(s^2+\omega_{res}^2\right)} \quad (1)$$

$$\omega_{res} = \sqrt{\left(L_i + L_g\right)/\left(C L_i L_g\right)} \quad (2)$$

$$G_c(s) = K_p + \frac{2\omega_i K_r S}{S^2+2\omega_i s+\omega_o^2} \quad (3)$$

where ω_o and ω_i are the fundamental frequency and the bandwidth of the resonant part of the PR regulator, respectively.

According to Fig. 2, the transfer function of the actively damped filter is expressed in (4).

$$F_{ad}(s) = \frac{1}{C L_g L_i S\left(S^2+\frac{H_d}{L_i}S+\omega_{res}^2\right)} \quad (4)$$

In Figs. 3(a) till 3(d), the capacitor-current-based active damping system is manipulated using signal flow graph manipulation. In Fig. 3(a), the capacitor current is replaced by the difference between the inverter output current and the grid injected current. With further manipulation, it is shown in Fig. 3(c) that the capacitor current feedback is equivalent to using three feedback loops of the grid current (i_g), the capacitor voltage (v_c), and the modulated inverter voltage (v_i). By further manipulation, the modulated voltage feedback is augmented in the main loop as a HPF, which is denoted as $G_h(s)$ and expressed in (5), with a cut off frequency of $\omega_h = H_d/L_i$; this system is shown in Fig. 3(d). The typical rang for ω_h can be calculated by expressing the transfer function of the actively damped filter (F_{ad}) in terms of ω_h and writing it in a standard form as in (6). The damping ratio ζ is typically around 0.7 [8], [21]. Therefore, the typical range for ω_h can be determined as $\omega_{res} < \omega_h < 2\omega_{res}$.

$$G_h(s) = \frac{1}{\omega_h} \cdot \frac{s}{1+s/\omega_h} \quad (5)$$

$$F_{ad}(s) = \frac{1}{C L_g L_i S\left(S^2+\omega_h S+\omega_{res}^2\right)} = \frac{1}{C L_g L_i S\left(S^2+2\zeta\omega_{res} S+\omega_{res}^2\right)} \quad (6)$$

Note that the capacitor voltage feedback is an integrator, denoted as $G_i(s)$ in Fig. 3(d), with a time constant of L_i.

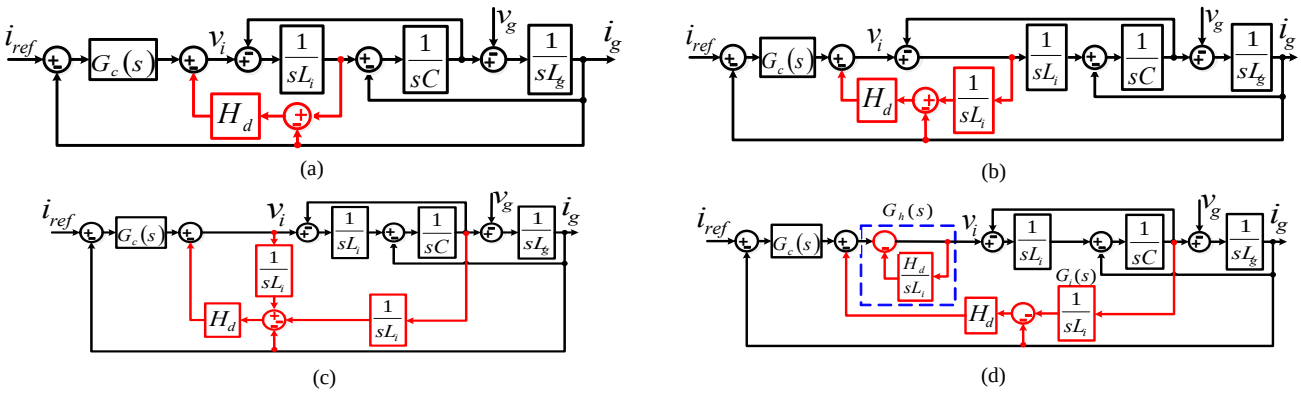

Fig. 3. Manipulation of the capacitor-current-based active damping technique.

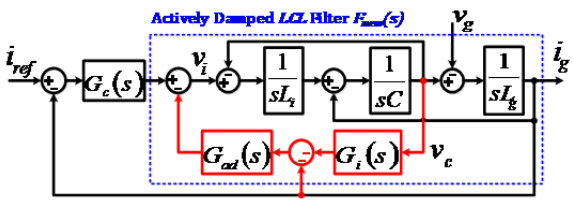

Fig. 4. Block diagram of the proposed active damping strategy.

The presence of the HPF (G_h) in cascade with the main control loop can deteriorate the system disturbance rejection capability. This deterioration can be determined by comparing the system transfer function to the grid voltage (v_g) for both the original system (shown in Fig. (2)) and the final manipulated system (shown in Fig. 3 (d)) considering the above-determined typical range of ω_h [21].

B. Proposed Active Damping System

The proposed system is derived in two steps as follow:

1. The HPF, G_h(s), is eliminated from the main control loop and only inserted in the active damping feedback loop to keep its damping effect. By multiplying G_h(s) by H_d, the resulted transfer function, G_{ad} (s) expressed in (7), is still a HPF with a gain of L_i. This system is shown in Fig. 4. Then, the new actively damped filter ($F_{new}(s)$) is expressed in (8).

$$G_{ad}(s) = \frac{sL_i}{1+s/\omega_h} \tag{7}$$

$$F_{new}(s) = \frac{G_{ig}(s)}{1-G_{ad}(s)G_{ig}(s)\left(1+sL_gG_i(s)\right)} = \frac{(1+s/\omega_h)}{s^2\left(\frac{CL_iL_g}{\omega_h}s^2+CL_iL_gs+\frac{(L_i+L_g)}{\omega_h}\right)} \tag{8}$$

The s^2 term in the denominator of $F_{new}(s)$ results in a constant phase of -180° in the open loop bode plot. This in turn, can dramatically deteriorate the phase margin. As a result, more modifications are necessary.

2. Both the gain of G_{ad}(s) and the time constant of G_i(s) are expressed in terms of a new variable (K_d) as in (9) and (10), respectively.

$$G_{ad}(s) = \frac{(K_d-L_g)s}{1+s/\omega_h} \tag{9}$$

$$G_i(s) = \frac{1}{(K_d-L_g)s} \tag{10}$$

Substituting (9) and (10) into (8), $F_{new}(s)$ is re-written as:

$$F_{new} = \frac{(1+s/\omega_h)}{CL_iL_gs(s^2+\omega_{res}^2)(1+s/\omega_h)-sK_d} = \frac{(1+s/\omega_h)}{\frac{CL_iL_g}{\omega_h}s^4+CL_iL_gs^3+\frac{L_i+L_g}{\omega_h}s^2+(L_i+L_g-K_d)s} \tag{11}$$

Using Routh's criteria, K_d has to follow the constraint in (12) to guarantee the open loop system stability and hence minimum phase behavior.

$$0 < K_d < (L_i + L_g) \tag{12}$$

To generalize the following analysis, K_d is expressed in terms of the above maximum limit $(L_i + L_g)$ as in (13), where $0 < \beta_d < 1$ for a stable open loop system.

$$K_d = \beta_d\,(L_i + L_g) \tag{13}$$

Substituting (13) into (11), the actively damped filter of the proposed system is finally expressed in (14).

$$F_{new}(s) = \frac{(1+s/\omega_h)}{CL_iL_gs(s^2+\omega_{res}^2)(1+s/\omega_h)-s\beta_d\,(L_i+L_g)} \tag{14}$$

III. DISCRETE IMPLEMENTATION

A. System Discretization

The discrete system representation of the proposed active damping strategy is shown in Fig. 5 where the DSP delay is represented by one sample delay. Using Tustin approximation with pre-warping at the fundamental frequency, the discrete *PR* regulator is determined in (15) where T_s is the sampling period.

$$G_c(z) = K_p + K_r\frac{sin(\omega_oT_s)}{2\omega_o}\frac{z^2-1}{(z^2-2z\,cos(\omega_oT_s)+1)} \tag{15}$$

In addition to G_{ig}(s), expressed in (1), two other transfer functions should be defined for system discretization:

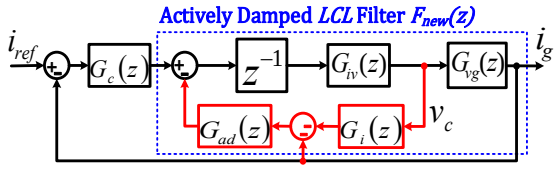

Fig. 5. Discrete representation of the proposed system.

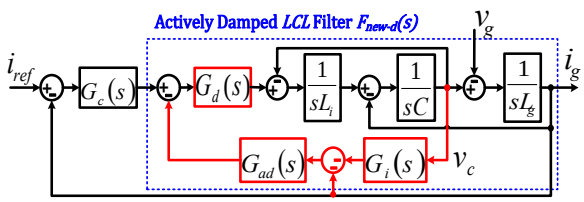

Fig. 6. System equivalent discrete implementation.

- G_{iv}(s), expressed in (16), is the transfer function relating the modulated inverter voltage to the filter capacitor voltage.
- G_{vg}(s), expressed in (17), is the transfer function relating the filter capacitor voltage to the grid current.

Using Zero-Order-Hold (ZOH) discretization, G_{ig}(z) and G_{iv}(z) are expressed as (18) and (19), respectively. G_{vg}(z) is determined as G_{ig}(z)/G_{iv}(z).

$$G_{iv}(s) = \frac{1}{CL_i(s^2+\omega_{res}^2)} \tag{16}$$

$$G_{vg}(s) = \frac{1}{sL_g} \tag{17}$$

$$G_{ig}(z) = \frac{T_s}{(L_i+L_g)}\left(\frac{(1-\alpha)z^2-2(cos(\delta)-\beta)z+(1-\alpha)}{(z-1)(z^2-2z\,cos(\delta)+1)}\right) \tag{18}$$

$$G_{iv}(z) = \frac{1}{L_iC\omega_{res}^2}\frac{(1-cos(\delta))(1+z)}{(z^2-2z\,cos(\delta)+1)} \tag{19}$$

where $\delta = \omega_{res}T_s$ and $\alpha = \frac{sin(\omega_{res}T_s)}{\omega_{res}T_s}$

For the active damping loops, G_i(z) and G_{ad}(z) are determined using Tustin approximation and expressed in (20) and (21), respectively.

$$G_i(z) = \frac{T_s}{2(K_d-L_g)}\frac{z+1}{z-1} \tag{20}$$

$$G_{ad}(z) = K_{ad}\frac{z-1}{z+\omega_{ad}} \tag{21}$$

where $K_{ad} = \frac{2\omega_h(\beta_d(L_i+L_g)-L_g)}{\omega_hT_s+2}$ and $\omega_{ad} = \frac{\omega_hT_s-2}{\omega_hT_s+2}$

Finally, the discrete actively damped filter and the loop transfer function are expressed in (22) and (23), respectively.

$$F_{new}(z) = \frac{z^{-1}G_{ig}(z)}{1-z^{-1}G_{ig}(z)G_{ad}(z)(1+G_i(z)/G_{vg}(z))} \tag{22}$$

$$T_{loop}(z) = G_c(z)F_{new}(z) \tag{23}$$

B. Control Parameters Design

For tuning purpose, the equivalent *s*-domain representation, shown in Fig. 6, is used. The DSP delay is modelled by an exponential transfer function of $G_d(s) = e^{-1.5sT_s}$ [9]. According to this representation, both the actively damped filter transfer function (F_{new-d}) and the loop transfer function (T_{loop-d}) are expressed in (24) and (25), respectively.

$$F_{new-d}(s) = \frac{(1+s/\omega_h)G_d(s)}{CL_iL_gs(s^2+\omega_{res}^2)(1+s/\omega_h)-s\beta_d(L_i+L_g)G_d(s)} \tag{24}$$

$$T_{loop-d}(s) = G_c(s)F_{new-d}(s) \tag{25}$$

It was shown in [12] that the resonant frequency changes with discrete implementation. The new resonant frequency will be denoted as ω_{res-ad}. At this resonant frequency the gain of F_{new-d} can be approximately expressed in (26).

$$|F_{new-d}(j\omega_{res-ad})| \cong \left|\frac{(1+j\omega_{res-ad}/\omega_h)}{-j\omega_{res-ad}\beta_d(L_i+L_g)}\right| \tag{26}$$

According to (26), higher values of ω_h should be used to acquire better damping effect. Theoretically, for discrete implementation, ω_h can be extended up to $0.5\omega_s$ (Nyquist sampling theory, where ω_s is the control frequency in rad/sec). However, such high value can deteriorate the discretization process. A value of $\omega_h = 0.4\omega_s$ is adopted here.

Since the resonant gain of the *PR* regulator is mainly effective at the fundamental frequency, the PR controller can be approximated as (27)

$$G_c(j\omega) = \begin{cases} K_p & for \quad \omega > \omega_o \\ K_r & for \quad \omega = \omega_o \end{cases} \tag{27}$$

At the crossover frequency (ω_c), which should be sufficiently higher than ω_o and below both ω_{res} and the adopted ω_h ($0.4\omega_s$), the loop gain can be approximated as (28).

$$T_{loop-d}(j\omega_c) = \frac{K_p}{\omega_c(L_i+L_g)}\frac{e^{-j1.5T_s\omega_c}}{(1-\beta_de^{-j1.5T_s\omega_c})}$$

$$|T_{loop-d}(j\omega_c)| = \frac{K_p}{\omega_c(L_i+L_g)}\left|\frac{1}{(1-\beta_de^{-j1.5T_s\omega_c})}\right| = 1 \tag{28}$$

Using Trigonometry, this gain is reduced to (29).

$$|T_{loop-d}(j\omega_c)| = \frac{K_p}{\omega_c(L_i+L_g)}\left|\frac{1}{A_ce^{j\theta_c}}\right| = \frac{K_p}{\omega_c(L_i+L_g)A_c} = 1 \tag{29}$$

where

$$A_c = \sqrt{1+\beta_d^2-2\beta_d^2\cos(1.5T_s\omega_c)}$$

$$\theta_c = \sin^{-1}\frac{\beta_d\sin(1.5T_s\omega_c)}{A_c} \tag{30}$$

Hence, for certain value of β_d, K_p should be calculated as in (31) to obtain certain crossover frequency.

$$K_p = \omega_c(L_i+L_g)A_c \tag{31}$$

Substituting (31) into (23), the loop transfer function is expressed in (32)

$$T_{loop}(z) = A_c\omega_c(L_i+L_g)F_{new}(z) \tag{32}$$

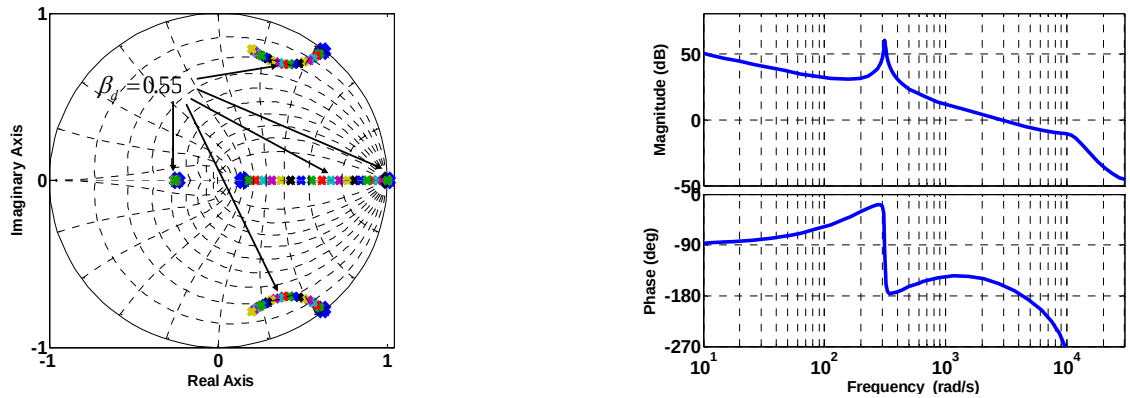

(a) (b)

Fig. 7. (a) pole-map of $F_{new}(z)$ for ω_{res1}=0.143ω_s with sweeping β_d (b) corresponding bode plot for T_{loop} at β_d =0.55.

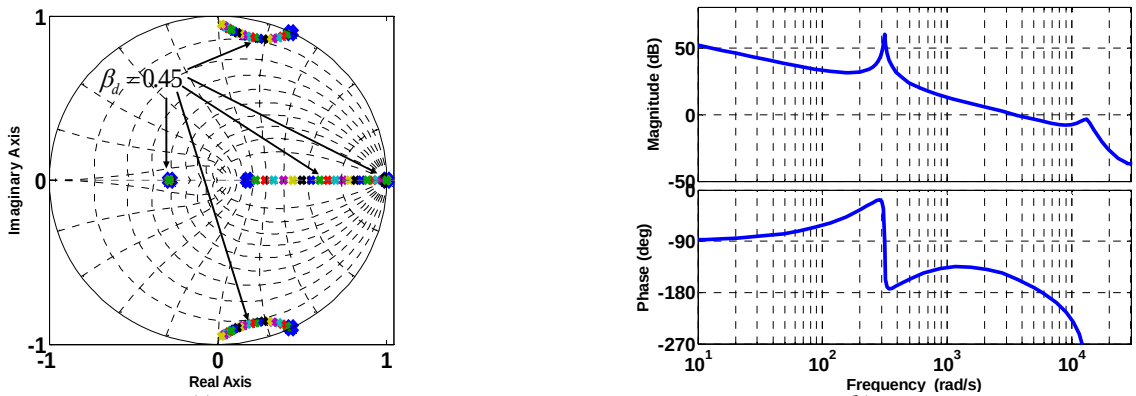

(a) (b)

Fig. 8. (a) pole-map of $F_{new}(z)$ for ω_{re2} =0.179ω_s with sweeping β_d, (b) corresponding bode plot for T_{loop} at β_d =0.45.

At the fundamental frequency, the loop gain can be approximated as in (33).

$$\left|T_{loop-d}(j\omega_o)\right| = \frac{K_r}{\omega_o(L_i+L_g)A_o} \tag{33}$$

where $A_o = \sqrt{1+\beta_d^2-2\beta_d^2\cos(1.5T_s\omega_o)}$

This is expressed in dB in (34) from which K_r can be determined from (35) for certain fundamental loop gain (T_{fo}).

$$T_{fo} = 20\log_{10}\frac{K_r}{\omega_o(L_i+L_g)A_o} \tag{34}$$

$$K_r = \omega_o(L_i+L_g)A_o\cdot 10^{\frac{T_{fo}}{20}} \tag{35}$$

Using the above-derived expressions, the following steps are proposed to co-design the control system parameters.

1. Plot the pole map of $F_{new}(z)$, expressed in (22), by sweeping β_d. Select β_d so that it corresponds to the farthest resonant poles inside the unit circle to achieve the best damping.
2. For a certain value of the fundamental loop gain (T_{fo}) along with the selected value for β_d, use (35) to determine K_r.
3. For a certain value of the crossover frequency (ω_c) along with the selected value of β_d, use (31) to determine K_p.
4. Plot a bode diagram for the loop transfer function expressed in (23). Check the resonant peak. If the resonant peak is more than 0 dB, then decrease the pre-specified crossover frequency (ω_c) and repeat steps 3 and 4.

IV. VERIFICATION

A. Numerical Example

Table I lists the parameter values of the grid-connected inverter shown in Fig. 1. Four capacitance values, corresponding to resonant frequencies of 0.143ω_s, 0.179ω_s, 0.209ω_s and 0.241ω_s are used to verify the performance of the proposed system over a wide range of resonant frequencies with respect to the control frequency. These resonant frequencies are denoted as ω_{res1}, ω_{res2}, ω_{res3} and ω_{res4}, respectively. The HPF cut off frequency (ω_h) value is taken as 0.4ω_s to mitigate the resonant peak as much as possible. In addition, a value of 60 dB is adopted for the fundamental loop gain (T_{fo}). Finally, an initial value for the crossover frequency of 0.3 of each corresponding resonant frequency is adopted.

Using the tuning steps presented in the last section, a pole-map of $F_{new}(z)$ is plotted with variation of β_d. These pole maps are plotted in Figs. 7(a), 8(a), 9(a) and 10(a) for the resonant frequencies ω_{res1}, ω_{res2}, ω_{res3} and ω_{res4}, respectively. To achieve the best damping effect, the values of β_d corresponding to the farthest resonant poles inside the unit circle are selected. These values are determined as 0.55, 0.45, 0.3 and 0.15 for ω_{res1}, ω_{res2}, ω_{res3} and ω_{res4}, respectively. Using the selected values of β_d along with the pre-specified values of ω_c and T_{fo}, the corresponding values of K_p and K_r are determined from (31) and (35), respectively.

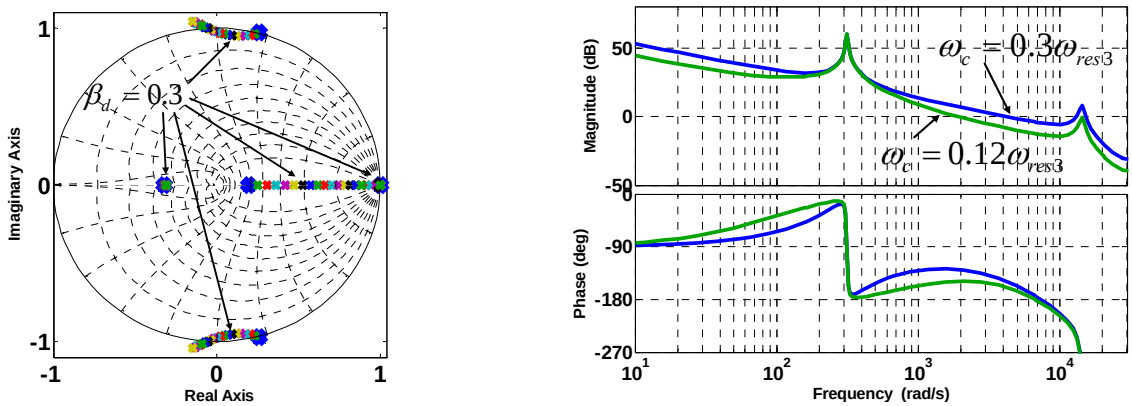

(a) (b)

Fig. 9. (a) pole-map of $F_{new}(z)$ for ω_{re3} =0.209ω_s with sweeping β_d, (b) corresponding bode plot for T_{loop} at β_d =0.3 and different crossover frequencies.

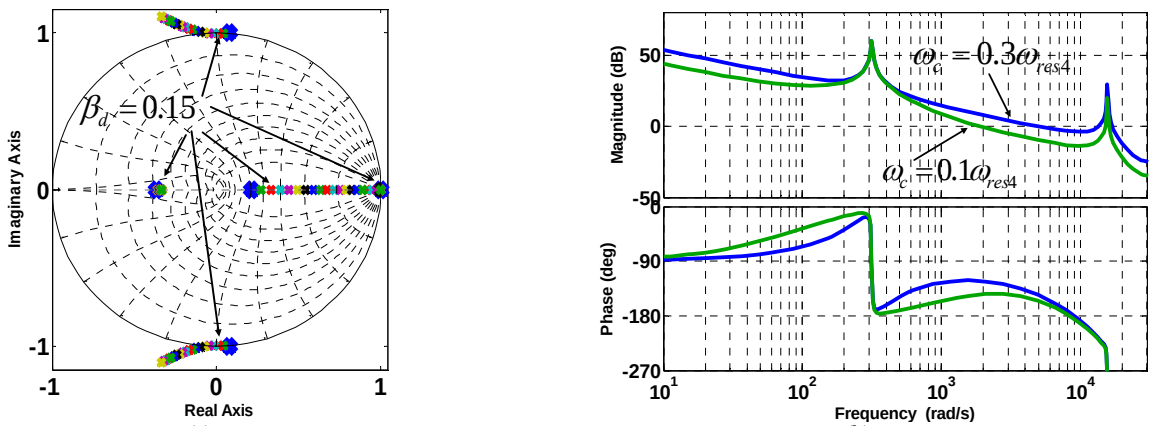

(a) (b)

Fig. 10. (a) pole-map of $F_{new}(z)$ for ω_{re4}=0.241ω_s with sweeping β_d, (b) corresponding bode plot for T_{loop} at β_d =0.15 and different crossover frequencies.

TABLE I

SYSTEM PARAMETERS

Symbol	Quantity	Value
P	Rated power	400 W
V_g	Grid voltage	100 V
F_o	Grid Frequency	50 Hz
V_{dc}	DC Voltage	200 V
L_i	Inverter side inductance	1.85 mH
L_g	Grid side inductance	1.3 mH
C	Capacitance	16.3 µF, 10.4 µF, 7.6 µF, 5.7 µF
F_{sw}	Switching Frequency	10 KHz
F_s	Sampling Frequency	10 KHz

For ω_{res1} and ω_{res2}, Figs. 7(b) and 8(b) show bode plots of the loop transfer function, expressed in (23), respectively. It is shown that the resonance peak is less than 0 dB. For ω_{res3} and ω_{res4}, it is found that the frequency response exhibits a resonant peak of more than of 0 dB. To overcome this issue, a reduction in the crossover frequency has to be adopted. For ω_{res3}, it is found that a reduction of the crossover frequency of 0.12ω_{res3} can reduce the resonant peak to less than 0 dB However, for ω_{res4}, a large crossover frequency reduction is required to obtain a resonant peak of less than 0 dB. Such a reduction can deteriorate the system dynamic performance.

Moreover, the phase lag introduced by the PR controller at low frequencies dramatically reduces the phase margin. Therefore, only a reduction of the crossover frequency to 0.1ω_{res4} is adopted. Figs. 9(b) and 10(b) show the frequency responses for ω_{res3} and ω_{res4}, respectively.

Table II summaries the designed control parameters and the achieved performance of the phase margin (PM), ω_c and T_{fo}. These results indicate the well damped performance of the proposed method over a wide range of resonant frequencies while meeting the pre-specified values of ω_c and T_{fo}.

B. Robustness against Grid Inductance Variations

In real operation, the grid side inductance (L_g) may vary significantly. To investigate system robustness against such variations, the pole maps of the closed loop system T_{closed}, expressed in (36), are plotted in Fig. 11 while sweeping L_g between 100-300% of its original value.

$$T_{closed}(z) = \frac{T_{loop}(z)}{1+T_{loop}(z)} \tag{36}$$

For the considered resonant frequencies, it is shown that the closed loop poles move inside the unit circle with an increasing L_g. These plots reflect the system robustness against grid inductance variations.

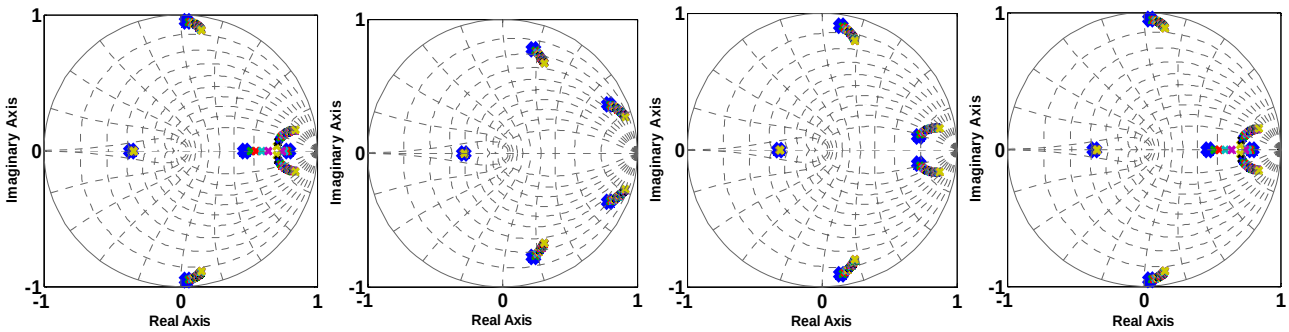

(a) (b) (c) (d)

Fig. 11. Closed loop pole maps with grid inductance (L_g) variation for (a) ω_{res1}=0.143ω_s, (b) ω_{res2}=0.179ω_s, (c) ω_{res3}=0.201ω_s, (d) ω_{res4}=0.241ω_s.

TABLE II
DESIGNED CONTROL PARAMETERS & FREQUENCY RESPONSE RESULTS

C (μF)	Assumed ω_c (rad/sec)	Designed Parameters			Achieved frequency response		
		β_d	K_r	K_p	ω_c (rad/sec)	PM (degree)	T_{lo} (dB)
16.3	0.3ω_{res1}	0.55	446	4.57	0.32ω_{res1}	19.9	60.1
10.4	0.3ω_{res2}	0.45	545	6.83	0.31ω_{res2}	25.2	60.1
7.6	0.3ω_{res3}	0.3	693	9.54	0.32ω_{res3}	31.2	60.1
	0.12ω_{res3}			3.53	0.14ω_{res3}	31.5	60
5.7	0.3ω_{res4}	0.15	841	12.73	0.32ω_{res4}	35.2	60.1
	0.1ω_{res4}			4.08	0.12ω_{res4}	35.1	60

C. Comparative Study

To show the superiority of the proposed method compared to the existing capacitor voltage/current based AD methods, the limitations of these methods are clarified under the same parameters used in the aforementioned numerical example.

- *Capacitor-voltage-based AD method*: Fig. 12 shows a discrete representation of this method, where a lead-lag network of $G_{ad\text{-}v}(z)$ is used for AD. The s-domain counterpart of this network is expressed as $G_{ad\text{-}v}(s)$ in (37). Using Fig. 12, the discrete loop transfer function can be expressed as (38). It was demonstrated in [17] that this method can behave effectively over the limited range of resonant frequencies between 1/3.2 and 1/3.4 of the sampling frequency (ω_s). To emphasize the difficulty of using this method outside specified limits, the AD loop design procedures presented in [17] are used for the resonant frequencies ω_{res1} and ω_{res2} ($<\omega_s/3.2$) as follows. The value of K_f is determined using (39) to achieve a maximum network angle (φ_{max}) of 75 degree at a frequency of $\omega_{max} = \omega_{res}$. Then, the minimum value of K_d is determined as $(K_{dmin} = L_g/3T_s)$. Following this, the root locus of the closed loop system, expressed in (40), is plotted while sweeping K_d (starting the from K_{dmin}) as shown in Figs. 13(a) and 13(b) for the resonant frequencies ω_{res1} and ω_{res2}, respectively.

$$G_{ad-v}(s) = K_d C \omega_{res} \frac{s+K_f\omega_{res}}{K_f s+\omega_{res}} \quad (37)$$

$$T_{open-v}(z) = \frac{z^{-1}G_c(z)G_{iv}(z)G_{vg}(z)}{1+z^{-1}G_{ad-v}(z)G_{iv}(z)} \quad (38)$$

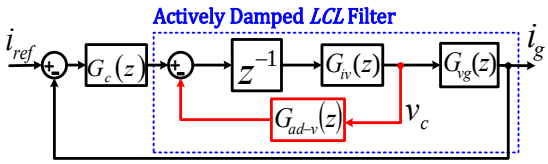

Fig. 12. Block representation of capacitor-voltage-based AD method.

$$K_f = \sqrt{\frac{1-\sin\varphi_{max}}{1+\sin\varphi_{max}}} \quad (39)$$

$$T_{closed-v}(z) = \frac{T_{open-v}(z)}{1+T_{open-v}(z)} \quad (40)$$

It is shown in these plots that the system cannot be stable for any values of K_d. This ensures the difficulty of using this method for resonant frequencies outside specific limits. On the other hand, the proposed method behaves effectively over a wide range of resonant frequencies as verified in the above numerical example.

- *Capacitor-Current-based AD Method*: In addition to its need for a high cost current sensor or a complicated observer loop to measure or estimate the capacitor current, it was shown in [12] and [13] that non-minimum phase behavior cannot be avoided for resonant frequencies of more than one-sixth of the sampling frequency, which implies an ineffective active damping [11]. Moreover, it was demonstrated in [12] and [13] that closed loop systems can hardly be stable at resonant frequency equal to one-sixth of the sampling frequency. This value of the resonant frequency can likely be reached due to grid inductance variations, which in turn implies a weak robustness. To emphasize these limitations, the capacitor- current-based AD method is used for the resonant frequencies ω_{res2} and ω_{res3} ($>\omega_s/6$). As shown in Fig. 2, the discrete closed loop system of this method can be easily derived and denoted as $T_{closed\text{-}c}$. To verify the system robustness, the pole map of $T_{closed\text{-}c}$ is plotted while sweeping L_g between 100-300% of its original value. These plots are shown in Figs. 14(a) and 14(b) for ω_{res2} and ω_{res3}, respectively (The control parameters are determined using the procedures presented in

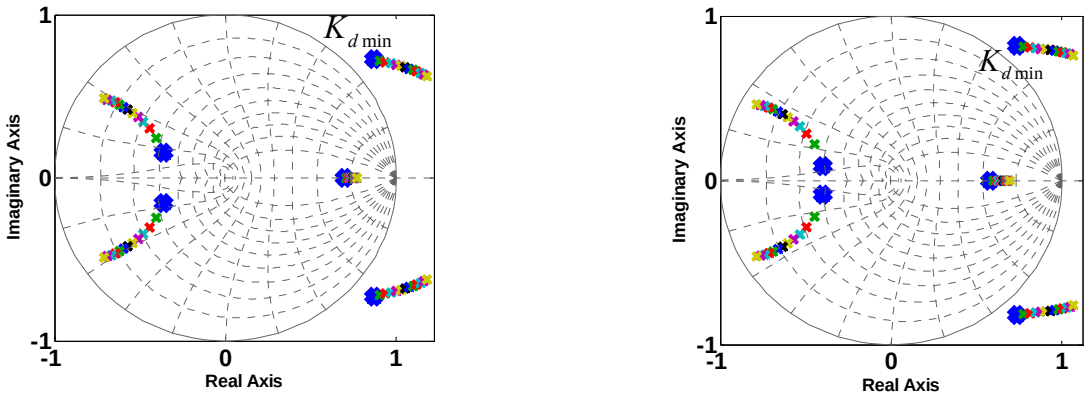

(a) (b)

Fig. 13. Closed loop pole map using capacitor-voltage-based AD method with sweeping K_d, a) for ω_{res1}=0.143ω_s (K_p=8.47), b) for ω_{res2}=0.179ω_s (K_p=10.6).

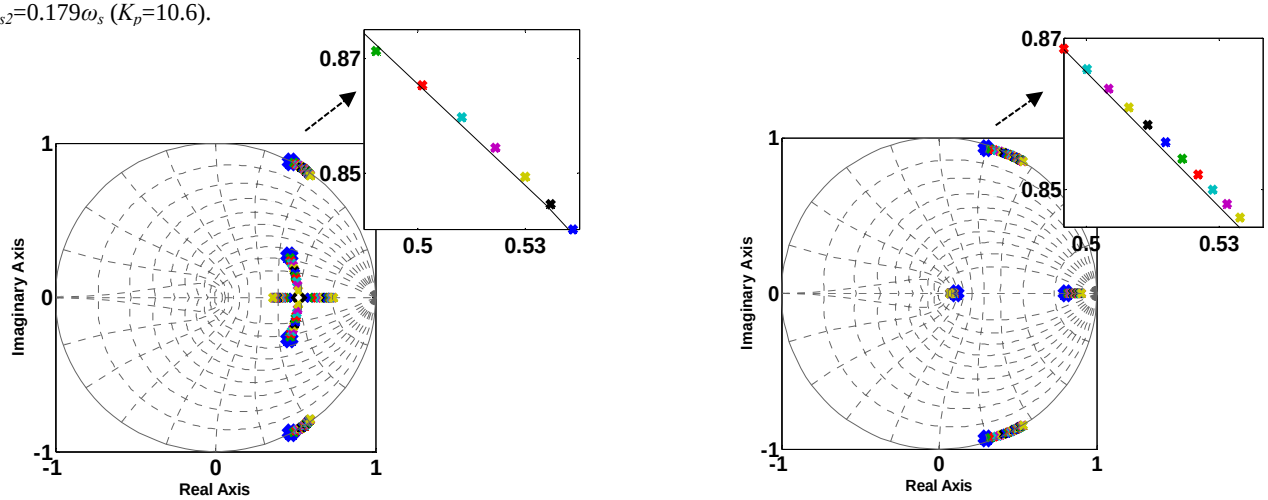

(a) (b)

Fig. 14. Closed loop pole map of capacitor-current-based AD method with sweeping L_g, a) for ω_{res2} (K_p=10.6, H_d=5) , b) for ω_{res3} (K_p=4.96, H_d=1).

[9] and listed in below the corresponding plots). It is shown that the closed loop poles are very close to the unit circle. This in turn, demonstrates the ineffective damping performance of this method for resonant frequencies of more than one-sixth of the sampling frequency. Moreover, as shown in the zoomed part, the system stability violates around a certain value of the grid inductance corresponding to a resonant frequency of one-sixth of the sampling frequency. On the other hand, it has been shown that avoiding such non-minimum behavior and high robustness against grid inductance variations can be achieved over a wide range of resonant frequencies using the proposed AD method.

D. Experimental Work

Using the system parameters listed in Table I, a single phase inverter prototype has been built and connected through an *LCL* filter to an AC power supply to emulate a grid. The control algorithm has been implemented using the PE-Expert3 platform, which consists of a C6713-A DSP development board along with a high-speed PEV board for analog-to-digital conversion and PWM signal generation. To verify the dynamic response, the reference current is stepped up from 2 A (0.5I_{rated}) to 4 A (I_{rated}). Using the designed parameters listed in Table II, some tests are carried out with and without the proposed active damping method.

For ω_{res1}, which is lower than one-sixth of the sampling frequency, the system cannot be stabilized without active damping (AD). Thus, removing the active damping loop for this case causes a high oscillatory current as shown in Fig. 15(a). On the other hand, Fig. 15(b) shows the waveforms when using active damping loops.

For ω_{res2}, ω_{res3} and ω_{res4}, the system can be stabilized without active damping as shown in Figs. 16(a), 17(a) and 18(a). However, it can recognize the dynamic oscillations which are caused by weak damping (there is some damping introduced by the small resistance of the coils). Figs. 16(b), 17(b) and 18(b) show the waveforms when using the proposed active damping loops. It can recognize the mitigation effect of the dynamic oscillations when using the proposed active damping method. This mitigation effect can be further clarified in Figs. 19 and 20. These figures show the spectrum of the grid current for each resonant frequency with and without the proposed active damping method.

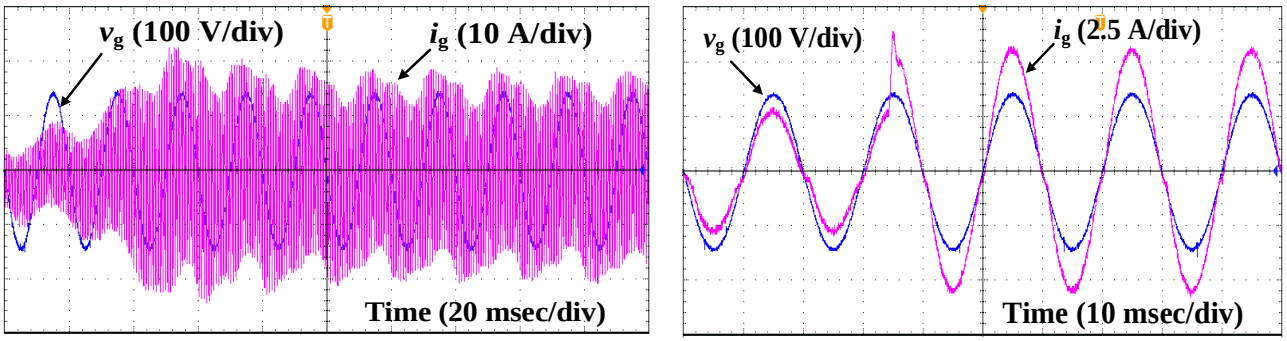

(a) (b)

Fig. 15. Experimental waveforms of grid current (i_g) and grid voltage (v_g) for ω_{res1} =0.143ω_s (a) without AD, (b) with AD.

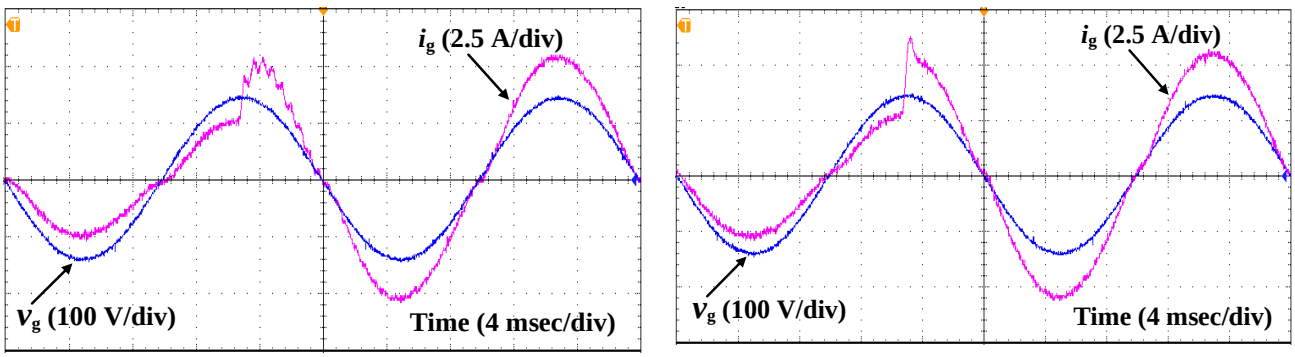

(a) (b)

Fig. 16. Experimental waveforms of grid current (i_g) and grid voltage (v_g) for ω_{res2} =0.179ω_s (a) without AD, (b) with AD.

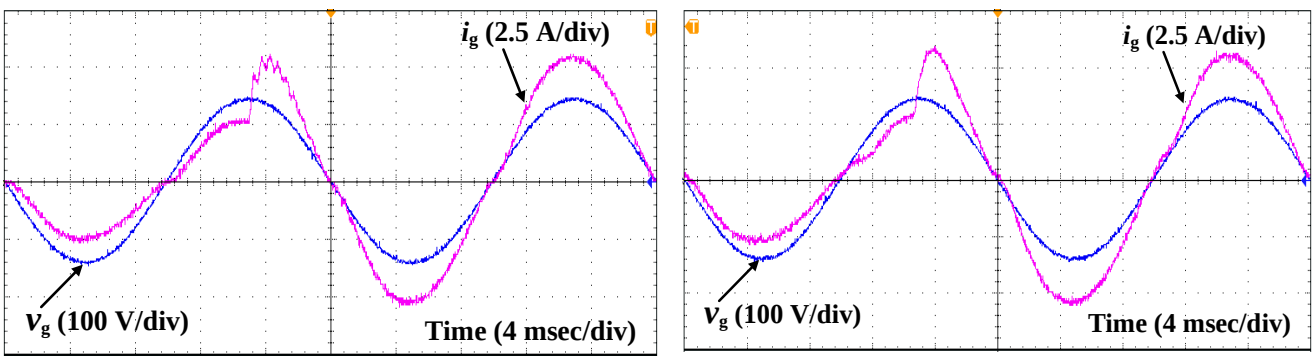

(a) (b)

Fig. 17. Experimental waveforms of grid current (i_g) and grid voltage (v_g) for ω_{res3} =0.209ω_s (a) without AD, (b) with AD.

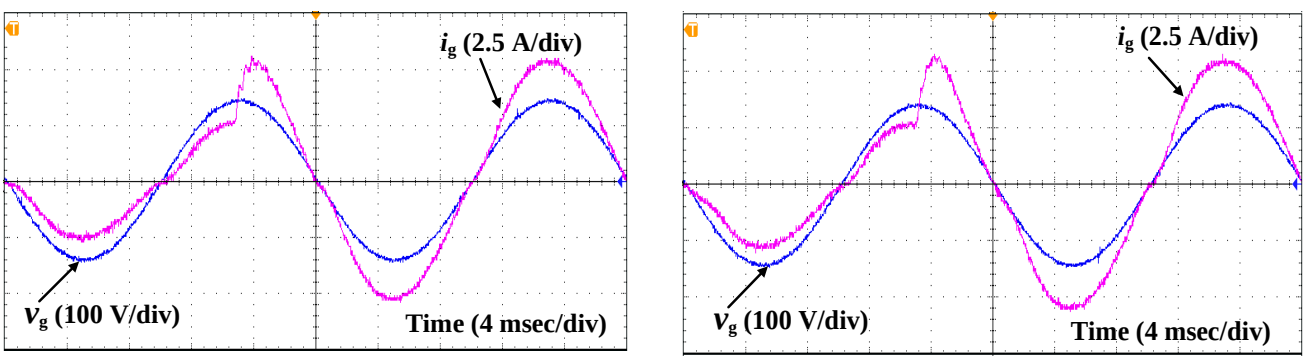

(a) (b)

Fig. 18. Experimental waveforms of grid current (i_g) and grid voltage (v_g) for ω_{res4} =0.241ω_s (a) without AD, (b) with AD.

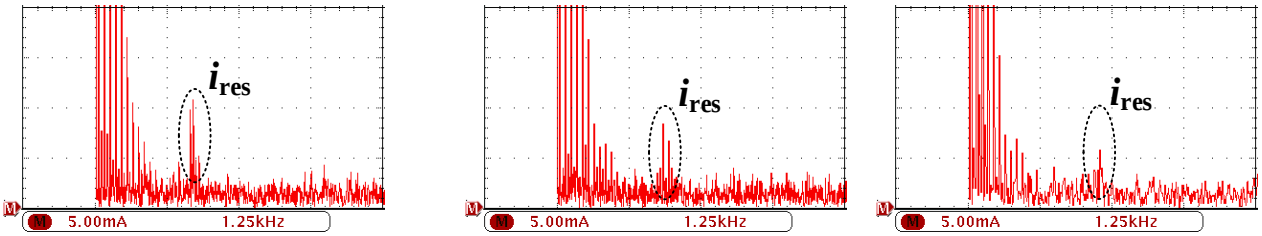

(a) (b) (c)

Fig. 19. Spectrum of the grid current (i_g) without active damping loops for (a) ω_{res2}=0.179ω_s (b) ω_{res3} =0.209ω_s and (c) ω_{res4}=0.241ω_s.

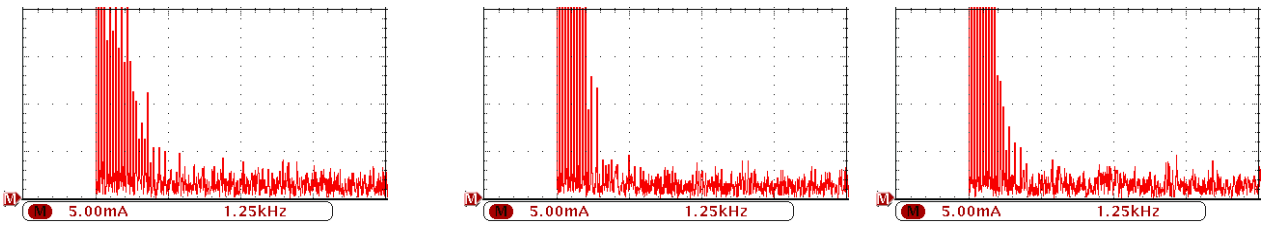

(a) (b) (c)

Fig. 20. Spectrum of the grid current (i_g) with active damping loops for (a) ω_{res2}=0.179ω_s (b) ω_{res3} =0.2ω_s and (c) ω_{res4}=0.241ω_s.

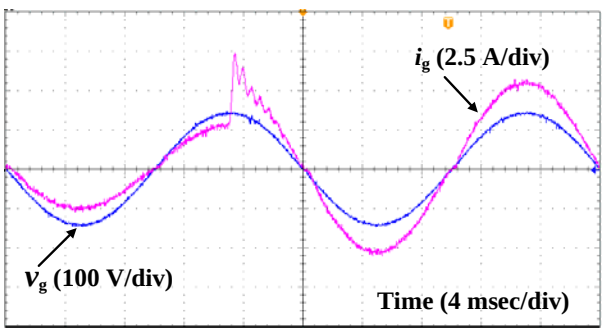

Fig. 21. Experimental waveforms of grid voltage (v_g) and grid current (i_g) using capacitor-current-based AD at ω_{res2} =0.179ω_s.

For experimental verification of its ineffective damping for resonant frequencies of more than one-sixth of the sampling frequency, the capacitor current based AD method has been used for the resonant frequency ω_{res2} (=0.179ω_s), and Fig. 21 shows the corresponding experimental waveforms. It can be seen that the resonant current oscillations are still present in this case. On the other hand, the damping of the proposed AD method at the same resonant frequency has been clarified in Fig. 16(b).

These results, along with the frequency response analysis introduced in the above numerical example, reflect satisfactory steady state and transient performances along with resonance damping over a wide range of resonant frequencies using the proposed active damping method and the control parameters tuning steps.

V. CONCLUSION

A novel active damping strategy using two feedback loops of the grid current and filter capacitor voltage is proposed in this paper. Compared to the previous active damping methods, the proposed one can offer the following merits.

- Compared to the capacitor-current-based method, the cost can be reduced by omitting the high cost current sensor. Moreover, the non-minimum phase behavior can be avoided over a wide range of resonant frequencies.
- Compared to the capacitor-voltage-based method, the proposed strategy can behave effectively over a wide range of the resonant frequencies without stability violations.
- Compared to the grid current based method, a straightforward co-design method for the fundamental current regulator and the active damping loops are proposed.

A numerical example has been introduced to verify the performance of the proposed method over a wide range of resonant frequencies. To show the superiority of the proposed method, the drawbacks of the capacitor voltage/current based methods have been clarified. This example along and experimental results reflect the satisfactory performance of the proposed method.

REFERENCES

[1] T. M. Blooming, and D. J. Carnovale, "Application of IEEE Std. 519-1992 harmonic limits," in *Pulp and Paper Industry Technical Conference, 2006. Conference Record of Annual*, pp. 1-9, 2006.

[2] J. Wang, J. D. Yan, L. Jiang, and J. Zou, "Delay-dependent stability of single-loop controlled grid-connected inverters with LCL filters," *IEEE Trans. Power Electron.,* Vol. 31, No. 1, pp. 743-757, Jan. 2016.

[3] X. Li, X. Wu, Y. Geng, and Q. Zhang, "Stability analysis of grid-connected inverters with an LCL filter considering grid impedance," *Journal of Power Electronics,* Vol. 13, No. 5, pp. 896-908, Sep. 2013.

[4] R.N. Beres, X. Wang, F. Blaabjerg, M. Liserre and C. L. Bak, "Optimal design of high-order passive-damped filters for grid-connected applications," *IEEE Trans. Power*

Electron., Vol. 31, No. 3, pp. 2083-2098, Mar. 2016.

[5] M. Huang, X. Wang, P. C. Loh and F. Blaabjerg, "Active damping of LLCL-filter resonance based on LC-trap voltage or current feedback," *IEEE Trans. Power Electron.,* Vol. 31, No. 3, pp. 2337-2346, Mar. 2016.

[6] J. Dannehl, M. Liserre, and F. W. Fuchs, "Filter-based active damping of voltage source converters with LCL filter," *IEEE Trans. Ind. Electron.,* Vol. 58, No. 8, pp. 3623-3633, Aug. 2011.

[7] W. Yao, Y. Yang, X. Zhang, and F. Blaabjerg, "Digital notch filter based active damping for LCL filters," in *Proc. of IEEE APEC*, pp. 2399-2406, 2015.

[8] C. Bao, X. Ruan, X. Wang, W. Li, D. Pan, and K. Weng, "Step-by-step controller design for LCL-type grid-connected inverter with capacitor–current-feedback active-damping," *IEEE Trans. Power Electron.,* Vol. 29, No. 3, pp. 1239-1253, Mar. 2014.

[9] S. G. Parker, B. P. McGrath, and D. G. Holmes, "Regions of active damping control for LCL filters," *IEEE Trans. Ind. Appl.,* Vol. 50, No. 1, pp. 424-432, Jan./Feb. 2014.

[10] Z. Wan, J. Xiong, J. Lei, C. Chen, and K. Zhang, "A Modified capacitor current feedback active damping approach for grid connected converters with an LCL filter," *Journal of Power Electronics,* Vol. 15, No. 5, pp. 1286-1294, Sep. 2015.

[11] X.Wang, F. Blaabjerg, P. C. Loh, "Virtual RC damping of LCL-filtered voltage source converters with extended selective harmonic compensation," *IEEE Trans. Power Electron.,* Vol. 30, No. 9, pp. 4726-4737, Sep. 2014.

[12] D. Pan, X. Ruan, C. Bao, W. Li, and X. Wang, "Capacitor-Current-Feedback active damping with reduced computation delay for improving robustness of LCL-type grid-connected inverter," *IEEE Trans. on Power Electron.,* Vol. 29, No. 7, pp. 3414-3427, July 2014.

[13] D. Pan, X. Ruan, C. Bao, W. Li and X. Wang, "Optimized Controller design for LCL-type grid-connected inverter to achieve high robustness against grid-impedance variation," *IEEE Trans Ind. Electron.,* Vol. 62, No. 3, pp. 1537-1547, Mar. 2015.

[14] X. Li, X. Wu, Y. Geng, X. Yuan, C. Xia and X. Zhang, "Wide damping region for lcl-type grid-connected inverter with an improved capacitor-current-feedback method," *IEEE Trans. Power Electron.,* Vol. 30, No. 9, pp. 5247-5259, Sep. 2015.

[15] Z. Xin, X. Wang, P. C. Loh, F. Blaabjerg, "Enhanced stability of capacitor-current feedback active damping for LCL-filtered grid converters," in *Energy Conversion Congress and Exposition (ECCE)*, pp. 4729-4736, 2015.

[16] V. Miskovic, V. Blasko, T. M. Jahns, A. H. C. Smith, and C. Romenesko, "Observer-based active damping of LCL resonance in grid-connected voltage source converters," *IEEE Trans. Ind. Appl.,* Vol. 50, No. 6, pp. 3977-3985, Nov./Dec. 2014.

[17] R. P-Alzola, M. Liserre, F. Blaabjerg, R. Sebastián, J. Dannehl, and F. W. Fuchs, "Systematic design of the lead-lag network method for active damping in LCL-filter based three phase converters," *IEEE Trans. Ind. Informat.,* Vol. 10, No. 1, pp. 43-52, Feb. 2014.

[18] W. Gullvik, L. Norum, and R. Nilsen, "Active damping of resonance oscillationsin LCL-filters based on virtual flux and virtual resistor," in *Eur. Conf. Power Electron. Appl.*, pp 1-10, Sep.2–5,2007.

[19] J. Xu, S. Xie, and T. Tang, "Active damping-based control for grid-connected LCL-filtered inverter with injected grid current feedback only," *IEEE Trans. Ind Electron.,* Vol. 61, No. 9, pp. 4746-4758, Sept. 2014.

[20] X. Wang, F. Blaabjerg, and P. Chiang Loh, "Grid-Current-Feedback active damping for LCL resonance in grid-connected voltage source converters," *IEEE Trans. Power Electron.,* Vol. 31, No. 1, pp. 213-223, Jan. 2016.

[21] M. A. Gaafar, G. M. Dousoky and M. Shoyama,"New active damping method for LCL filter resonance based on two feedback system," in *Proc. of IEEE APEC*, pp. 2735-2741, 2016.

Mahmoud A. Gaafar was born in Qena, Egypt, in 1982. He received his B.Sc. and M.Sc. degrees in Electrical Engineering from Aswan University, Aswan, Egypt, in 2004 and 2010, respectively. He is currently working towards Ph.D. degree in the Graduate School of Information Science and Electrical Engineering, Kyushu University, Fukuoka, Japan. His current research interests include grid-connected converters and digital control strategies.

Emad M. Ahmed (S'08–M'12) received his B.Sc. and M.Sc. in Electrical Engineering from Aswan University, Aswan, Egypt in 2001 and 2006 respectively. He received his Ph.D. degree from Kyushu University, Fukuoka, Japan, in 2012. Currently, he is an Assistant Professor in the Department of Electrical Engineering, Faculty of Engineering, Aswan University, Aswan, Egypt. He is a member of Aswan Power Electronics and Applications Research Center (APEARC), Aswan, Egypt as well. His present research interests include applied power electronics especially in renewable energy applications, Micro-grids and fault tolerant control. Dr. Emad received Baek-Hyun Award from the Korean Institute of Power Electronics (KIPE) for his academic contribution in the field of power electronics in 2012. He is a member of IEEE Power Electronics Society (PELS), and IEEE Industrial Electronics Society (IES).

Masahito Shoyama received his B. S. in Electrical Engineering and his Dr. Eng. from Kyushu University, Fukuoka, Japan, in 1981 and 1986, respectively. He joined the Dept. of Electronics, Kyushu University as a Research Associate in 1986. He had been an Associate Professor since 1990, and he has been a Professor since 2010. Since 2009 he has been with the Dept. of Electrical Engineering, Faculty of Information Science and Electrical Engineering, Kyushu University. He has been active in the field of power electronics, especially in the areas of bi-directional converters for DC/AC power systems, high-frequency switching converters for renewable energy sources, power factor correction (PFC) converters, and electromagnetic compatibility (EMC).